

## 1           **Functional Landscape of SARS-CoV-2 Cellular Restriction** 2

3       Laura Martin-Sancho<sup>1</sup>, Mary K. Lewinski<sup>2</sup>, Lars Pache<sup>1</sup>, Charlotte A. Stoneham<sup>2</sup>, Xin Yin<sup>1</sup>, Dexter  
4       Pratt<sup>3</sup>, Christopher Churas<sup>3</sup>, Sara B. Rosenthal<sup>3</sup>, Sophie Liu<sup>3</sup>, Paul D. De Jesus<sup>1</sup>, Alan M. O'Neill<sup>4</sup>, Anshu  
5       P. Gounder<sup>1</sup>, Courtney Nguyen<sup>1</sup>, Yuan Pu<sup>1</sup>, Aaron L. Oom<sup>2</sup>, Lisa Miorin<sup>5,6</sup>, Ariel Rodriguez-Frandsen<sup>1</sup>,  
6       Matthew Urbanowski<sup>5</sup>, Megan L. Shaw<sup>5,7</sup>, Max W. Chang<sup>3</sup>, Christopher Benner<sup>3</sup>, Matthew B. Frieman<sup>8</sup>,  
7       Adolfo García-Sastre<sup>5,6,9,10</sup>, Trey Ideker<sup>3,11</sup>, Judd F. Hultquist<sup>12</sup>, John Guatelli<sup>2</sup>, Sumit K Chanda<sup>1\*</sup>  
8

9       <sup>1</sup> Immunity and Pathogenesis Program, Infectious and Inflammatory Disease Center, Sanford Burnham  
10      Prebys Medical Discovery Institute, La Jolla, CA, USA

11      <sup>2</sup> Department of Medicine, University of California at San Diego, and the VA San Diego Healthcare  
12      System, San Diego, California, USA

13      <sup>3</sup> Department of Medicine, University of California San Diego, La Jolla, CA 92093, USA

14      <sup>4</sup> Department of Dermatology, University of California San Diego, La Jolla, CA 92093, USA

15      <sup>5</sup> Department of Microbiology, Icahn School of Medicine at Mount Sinai, New York, NY, USA

16      <sup>6</sup> Global Health and Emerging Pathogens Institute, Icahn School of Medicine at Mount Sinai, New York,  
17      NY, USA

18      <sup>7</sup> Department of Medical Biosciences, University of the Western Cape, Cape Town, South Africa

19      <sup>8</sup> Department of Microbiology and Immunology, University of Maryland at Baltimore, Baltimore,  
20      Maryland, USA

21      <sup>9</sup> Department of Medicine, Division of Infectious Diseases, Icahn School of Medicine at Mount Sinai,  
22      New York, NY, USA

23      <sup>10</sup> The Tisch Institute, Icahn School of Medicine at Mount Sinai, New York, NY, USA

24      <sup>11</sup> Department of Computer Science and Engineering, University of California San Diego, La Jolla, CA  
25      92093, USA

26      <sup>12</sup> Division of Infectious Diseases, Northwestern University Feinberg School of Medicine, Chicago, IL,  
27      60611, USA

28      33

29      34      \* Corresponding author:

30      35      Sumit K. Chanda

31      36      Sanford Burnham Prebys Medical Discovery Institute  
32      37      10901 North Torrey Pines Road, La Jolla, CA 92037, USA

33      38      E-mail: schanda@sbpdisccovery.org

34      39      Tel.: +1 (858)795-5241

35      40      Fax: +1 (858)795-5225

36      41

42 **SUMMARY**

43

44 A deficient interferon response to SARS-CoV-2 infection has been implicated as a determinant  
45 of severe COVID-19. To identify the molecular effectors that govern interferon control of SARS-CoV-  
46 2 infection, we conducted a large-scale gain-of-function analysis that evaluated the impact of human  
47 interferon stimulated genes (ISGs) on viral replication. A limited subset of ISGs were found to control  
48 viral infection, including endosomal factors that inhibited viral entry, nucleic acid binding proteins that  
49 suppressed viral RNA synthesis, and a highly enriched cluster of ER and Golgi-resident ISGs that  
50 inhibited viral translation and egress. These included the type II integral membrane protein  
51 BST2/tetherin, which was found to impede viral release, and is targeted for immune evasion by SARS-  
52 CoV-2 Orf7a protein. Overall, these data define the molecular basis of early innate immune control of  
53 viral infection, which will facilitate the understanding of host determinants that impact disease severity  
54 and offer potential therapeutic strategies for COVID-19.

55

56 **KEYWORDS:** SARS-CoV-2, innate immunity, interferon, ISG, BST2, Orf7a

57

58

59

60

61

62

63

64

65

66

67

68

69

70

71

72

73

74

75

76

77

78

79 **INTRODUCTION**

80 The ongoing coronavirus disease 2019 (COVID-19) pandemic, caused by severe acute respiratory  
81 syndrome coronavirus 2 (SARS-CoV-2), is responsible for a reported 23.5 million infections, and over  
82 800,000 deaths worldwide as of this writing (Dong et al., 2020). Following infection with SARS-CoV-  
83 2, COVID-19 clinical presentation ranges from asymptomatic or mild (suggested to account for ~ 80%  
84 of infections), to severe disease that typically requires hospitalization and assisted respiration (Huang et  
85 al., 2020). While age and co-morbidities, such as obesity and cardiovascular disease, have been linked  
86 to COVID-19 severity, recent data suggest that cellular immune responses to viral infection are also a  
87 critical determinant of disease outcome (Mathew et al., 2020). For instance, loss-of-function mutations  
88 in the immune sensor *TLR7* and downregulation of the type I interferon (IFN) response have been  
89 associated with severe COVID-19 (van der Made et al., 2020). In addition, two recent studies that  
90 conducted an integrated immune analysis of COVID-19 patients found impaired IFN responses in severe  
91 and critically ill patients (Arunachalam et al., 2020; Hadjadj et al., 2020). Further support for the role of  
92 IFN in COVID-19 outcome comes from a study of 127 patients receiving interferon beta-1b in  
93 combination with lopinavir–ritonavir and ribavirin, which reported lower SARS-CoV-2 viral load and  
94 shedding in the lungs and reduced length of hospitalization (Hung et al., 2020). Taken together, these  
95 data underscore an emerging role for IFN-mediated cellular responses in the control of SARS-CoV-2  
96 infection and COVID-19 severity.

97 Viral infection is sensed by pattern-recognition receptors (PRR), which initiate a signaling  
98 cascade that produces cytokines, including IFN. Binding of IFN to its receptor (IFNAR) promotes the  
99 transcriptional activation of hundreds of **interferon stimulated genes (ISGs)**, many of which exert  
100 antiviral activities (Schoggins et al., 2011). Concerted expression and regulation of these PRRs and  
101 downstream signaling molecules, transcription factors, and effectors are necessary to mount a successful  
102 antiviral response. Thus, viruses have developed various strategies to interfere with and evade these  
103 antiviral programs (García-Sastre, 2017). Recent work has shown that SARS-CoV-2 infection is  
104 sensitive to IFN treatment, as RNAseq of COVID-19 patients samples and *in vitro* infection models  
105 revealed upregulation of ISGs (Blanco-Melo et al., 2020; Emanuel et al., 2020; Lamers et al., 2020;  
106 Overmyer et al., 2020; Sun et al., 2020). In addition, the ISG *LY6E* has been identified as a negative  
107 regulator of SARS-CoV-2 (Pfaender et al., 2020), and the ISGs *AXIN2*, *CH25H*, *EPSTI1*, *GBP5*, *IFIH1*,  
108 *IFITM2*, and *IFITM3* were found to block entry of a pseudotyped vesicular stomatitis virus (VSV)  
109 harboring SARS-CoV-2 Spike (S) protein (Zang et al., 2020). Ultimately, a comprehensive evaluation  
110 of ISGs that inhibit infection of SARS-CoV-2 will be necessary to understand the cellular control of  
111 viral infection and their potential impact on COVID-19 outcome.

112 To uncover the cellular antiviral response to SARS-CoV-2 infection, we conducted a gain-of-  
113 function screen using 399 human ISGs. These data revealed that restriction of SARS-CoV-2 is mediated  
114 by a limited subset of 65 ISGs, most of which reside in the ER or Golgi compartments and function to

115 regulate endoplasmic reticulum-associated protein degradation (ERAD), lipid membrane composition,  
116 and vesicle transport. Among these was BST2, found to inhibit viral egress and to be antagonized by  
117 SARS-CoV-2 accessory protein Orf7a to rescue virion release. The identification of the ISG subset that  
118 direct the antiviral activity of IFN illuminates the molecular and genetic determinants of early immune  
119 regulation that contribute to COVID-19 outcome, and provide attractive specific targets for therapeutic  
120 intervention.

121 **RESULTS AND DISCUSSION**

122

123 **IFN-mediated restriction of SARS-CoV-2 relies on a limited subset of ISGs**

124 To define the cellular effectors that act to limit SARS-CoV-2 infection, we first sought to  
125 determine which genes are activated upon IFN stimulation (hereafter referred to as ISGs) in disease-  
126 relevant cell types. Human tracheobronchial epithelial (HTBE) and human alveolar epithelial A549 cells  
127 were treated with IFN for 8 h and then subjected to RNAseq. Using cut-off criteria of  $\log_{2}FC > 1.5$  and  
128 p value  $< 0.05$ , we identified 139 ISGs upregulated in HTBE, 121 ISGs upregulated in A549 cells, and  
129 152 ISGs upregulated in both HTBE and A549 (Fig S1A). This dataset encompassed ISGs with  
130 previously characterized broad-acting antiviral activities that included *MX1*, *OAS1*, *OASL* and *IFI6*  
131 (Hubel et al., 2019). In addition, Schoggins *et al.* previously assembled a list of 387 curated ISGs, of  
132 which 149 overlapped with the HTBE/A549 dataset (Fig S1B) (Schoggins et al., 2011). We combined  
133 these experimental and published datasets, and identified 399 ISGs as available, validated, and full-  
134 sequence length cDNA clones (Fig S1B, Table S1A, B).

135

136 Next, we evaluated the ability of these 399 ISGs to inhibit SARS-CoV-2 replication using  
137 ectopic expression screening. These studies were conducted using the human epithelial cell line 293T,  
138 as these cells can be transfected with high efficiencies and support productive replication of SARS-  
139 CoV-2 when expressing the viral entry factors *ACE2* and *TMPRSS2* (Hoffmann et al., 2020). 293T cells  
140 were transfected with individual ISGs along with *ACE2* and *TMPRSS2* for 30 h, and then challenged  
141 with SARS-CoV-2 at a low multiplicity of infection (MOI = 0.0625). Cells were fixed at 40 h post-  
142 infection, and infectivity was determined using immunostaining for SARS-CoV-2 nucleoprotein (N)  
143 (Fig 1A). cDNA encoding chloramphenicol acetyltransferase (*CAT*) was included on each plate as  
144 negative control, and cDNA encoding the SARS-CoV-2 negative regulator *LY6E* (Pfaender et al., 2020)  
145 was included as positive control (Fig 1A, B). Screens were conducted in duplicate and showed good  
146 reproducibility with a Pearson correlation coefficient ( $r$ ) = 0.81 (Fig 1C). After applying cut-off criteria  
147 for infectivity ( $\log_{2}FC$  at least four standard deviations lower than the *CAT* negative control) and cell  
148 viability (at least 70% number of cells of the negative control), we identified 65 ISGs that inhibited  
149 SARS-CoV-2 replication (Fig 1B). Cross-comparison of these 65 factors with published datasets of  
150 upregulated genes from COVID-19 patient samples and *in vitro* infected lung cell models revealed a  
151 significant overlap (Fig S1C), suggesting that these factors are also stimulated in response to SARS-

152 CoV-2 infection (Blanco-Melo et al., 2020; Emanuel et al., 2020; Overmyer et al., 2020; Sun et al.,  
153 2020).

154

155 To further validate the antiviral activity of the ISGs identified in this high-throughput screen,  
156 we generated stable cell lines expressing each of these 65 ISGs and assessed their ability to inhibit  
157 SARS-CoV-2 replication. Upon transduction of 293T-ACE2 cells with lentiviruses carrying these 65  
158 factors, 7 cell lines did not survive antibiotic selection, so stable lines could only be generated for the  
159 remaining 58 ISGs. Next, the ability of these ISG-expressing cells to support replication of SARS-CoV-  
160 2 was evaluated. Of these, 37 lines showed statistically significant reductions of SARS-CoV-2  
161 replication compared to parental cells ( $\log_{2}FC$  at least four standard deviations lower than parental cells  
162 and  $p$  value  $\leq 0.05$ ) (**Fig 1D, E**).

163

164 Importantly, this screening approach captured both upstream regulators as well as downstream  
165 effectors of the IFN response, including the signaling adaptor *MYD88*, signal transducers *STAT1* and  
166 *STAT2*, transcription factors *ELF1*, *REC8*, and *ETV6*, and several IFN effectors including *BST2*,  
167 *IFITM2*, and *IFITM3*, which likely harbor direct antiviral activities. The full list of identified ISGs and  
168 their activities are shown in **Table S2 and S3**.

169

## 170 Network model of SARS-CoV-2 antiviral effectors

171 ISGs are a heterogenous group of genes with encoded functions ranging from inflammatory  
172 pathway signaling to intracellular trafficking, energy metabolism, and nuclear transport (Schoggins,  
173 2019). To better understand the biochemical and functional context by which these 65 ISGs exert  
174 antiviral activities, we conducted a supervised network propagation leveraging high confidence protein-  
175 protein interactions and hierarchical relationships (**Fig 2**, see *Methods*). Using this analysis, we  
176 identified densely interconnected protein clusters that are significantly associated with cellular  
177 biological processes (Raudvere et al., 2019). As expected, we found strong association to pathways that  
178 stimulate IFN signaling, including cytosolic pattern recognition receptors and regulators of STAT  
179 phosphorylation, as well as pathways linked to the type I IFN response, the cellular response to viral  
180 infection, and cytokine signaling (**Fig 2A**, blue boxes). We also observed an enrichment of RNA  
181 helicases, and regulators of cell death. Within this group were *DDX60*, which exhibits antiviral activity  
182 against hepatitis C virus (HCV) and VSV (Schoggins et al., 2011), *ZBP1*, which was recently identified  
183 as a sensor of influenza A virus Z-RNA motifs, and *MKLK*, a ZBP1 binding partner and downstream  
184 activator of necroptosis in response of viral infection (**Fig 2B**) (Zhang et al., 2020). Additional enriched  
185 clusters included regulation of transport at the Golgi network or the ER (**Fig 2C, D**), nucleotide  
186 metabolism, and regulators of sphingolipid metabolism, including the ISGs *B4GALT5* and *ST3GAL4*  
187 (**Fig 2E**). Additional ER/Golgi resident factors identified as potent restrictors of SARS-CoV-2  
188 replication included the apolipoprotein *APOL2* and *RSAD2/Viperin*, which are involved in lipid

189 synthesis and mobilization. This suggests that regulation of the membrane composition at sites relevant  
190 for viral replication or trafficking is likely a critical host strategy for the control of SARS-CoV-2  
191 replication. Overall, this network analysis underscores the diversity of activities that underlie the cellular  
192 antiviral response to SARS-CoV-2 replication.

193

#### 194 **Restriction of SARS-CoV-2 entry**

195 To understand how these antiviral effectors impact viral replication, a selected subset of ISGs  
196 were tested for their ability to inhibit specific stages of the SARS-CoV-2 infectious cycle. Firstly, we  
197 adopted a pseudotyped VSV expressing SARS-CoV-2 S protein (VSV-S-luciferase) to measure *viral*  
198 *entry* (**Fig 3A**, diagram). Then we assessed *viral RNA replication* by measuring viral RNA at 8 h post-  
199 infection (**Fig 3B**). Lastly, we infected naïve cells with viral supernatants that were collected at 18 h  
200 post infection to assess *late stage activity*, encompassing viral translation and egress (**Fig 3C**). These  
201 experimental data were integrated with available bioinformatic resources that provided information on  
202 subcellular localization and known function to establish a predictive map of the impact of these ISGs on  
203 the SARS-CoV-2 infectious cycle (**Fig 4**).

204

205 Entry of SARS-CoV-2 into the host cell is facilitated by viral S protein binding to the ACE2  
206 cellular receptor promoting endocytosis. Upon entry, SARS-CoV-2 viral particles escape the endosome  
207 to initiate viral replication (Hoffmann et al., 2020). Six ISGs reduced entry of the pseudotyped VSV-S  
208 by more than 50%, including *LY6E*, *CLEC4D*, *UBD*, *ELF1*, *FAM46C* and *REC8* (**Fig 3A, 4**). *LY6E* was  
209 previously demonstrated to restrict SARS-CoV-2 entry by inhibiting viral S protein fusion at the  
210 membrane (Pfaender et al., 2020). *CLEC4D* is an integral membrane protein that acts as an endocytic  
211 receptor and has been linked to inhibition of bacteria uptake (Wilson et al., 2015). Another ISG affecting  
212 viral entry was *UBD/FAT10*, which is recruited to the incoming Salmonella-containing vacuole (SCV)  
213 together with the autophagy cargo receptor p62 (Spinnenhirn et al., 2014), and these serve as signals for  
214 lysosomal targeting and pathogen clearance. Since these ISGs have been reported to impact endo-  
215 lysosomal function, it is possible that they interfere with SARS-CoV-2 entry by impeding low pH-  
216 dependent entry or endosomal escape. Finally, the transcription factor *ELF1* was also found to affect  
217 viral entry. *ELF1* governs a complex transcriptional program of over 300 genes that are largely distinct  
218 from those induced by IFN, suggesting that a secondary antiviral transcriptional cascade acts to inhibit  
219 SARS-CoV-2 entry, and potentially other stages of the viral life cycle (Seifert et al., 2019).

220

#### 221 **Cellular inhibition of SARS-CoV-2 RNA replication**

222 Following SARS-CoV-2 release into the cytosol, expression of the replicase gene from the viral  
223 genomic RNA generates non-structural proteins (nsps). These nsps coordinate the assembly of the  
224 replicase-transcriptase complex (RTC) at the ER, which enables viral RNA replication and protein  
225 synthesis (Fehr and Perlman, 2015). Seven ISGs were found to strongly inhibit SARS-CoV-2 RNA

226 replication (>50% inhibition) (**Fig 3B**), including *IFIT3*, *SPATS2L*, *DNAJC6*, *RGSS2*, *LOC152225*, as  
227 well as *ZBP1* and *B4GALT5*, which were found to be core components of the cell death and sphingolipid  
228 metabolism networks shown in **Fig 2B, E**.

229

230 The IFIT-family includes five members (*IFIT1*, *IFIT1B*, *IFIT2*, *IFIT3*, and *IFIT5*), which  
231 prevent active viral RNA replication by detection and sequestering of single-stranded 5'-ppp or 2' O-  
232 unmethylated RNA (Metz et al., 2013). In this study, we identified three members of this family, *IFIT1*,  
233 *IFIT3*, and *IFIT5*, to inhibit SARS-CoV-2 replication, suggesting this family plays an important role in  
234 the restriction of SARS-CoV-2. RNA replication was also reduced by the RNA binding protein  
235 *SPAT2SL*. Following stress stimuli, SPAT2SL is recruited to cytoplasmic stress granules, where viral  
236 RNA can be sequestered to reduce viral genome synthesis (Miller, 2011; Zhu et al., 2008). Finally, the  
237 ISG *DNAJC6*, a member of the heat shock protein 40 (HSP40) family, was also determined to impact  
238 the SARS-CoV-2 replicative stage (**Fig 3B**). HSP40 family members are known to play critical roles in  
239 protein transport, folding, and structural disassembly, and can bind the 3' untranslated region of the  
240 mouse hepatitis virus (MHV) coronavirus (Nanda et al., 2003; Rosenzweig et al., 2019). Overall, these  
241 data suggest that molecular recognition and targeting of viral RNA is a critical host defense strategy  
242 used to interfere with SARS-CoV-2 genome synthesis.

243

#### 244 ER- and Golgi resident ISGs inhibit late stage SARS-CoV-2 replication

245 Transcription and translation of SARS-CoV-2 subgenomic mRNAs at the ER membrane  
246 generate accessory, as well as the structural proteins S, envelope (E), membrane (M), and nucleocapsid  
247 (N). S, E, and M are then inserted into the ER and transit through the secretory pathway to commence  
248 viral assembly in the ER–Golgi intermediate compartment (ERGIC). Specifically, M, S and E associate  
249 with viral genomes encapsidated by the N protein to form virions that bud from the ERGIC. Virions  
250 traffic in vesicles through the *trans*-Golgi network and are subsequently released by exocytosis. Notably,  
251 we found that a majority of ISGs in our assay (16/35, 55%) restricted late stages of viral replication (**Fig**  
252 **3C**). Based on their reported function, late stage ISGs were clustered with predicted impacts on  
253 translation, ERAD, and vesicle trafficking.

254

255 *Translation*. The 5'-nucleotidase family member *NT5C3*, as well as the broad spectrum antiviral *ISG20*,  
256 impacted translation or egress of SARS-CoV-2. While reported activities include regulation of  
257 nucleotide pools and RNA degradation, both factors have also been implicated in the inhibition of viral  
258 translation. Specifically, *NT5C3* was found to inhibit translation of HCV proteins, and *ISG20* was shown  
259 to interfere with translation of VSV by discriminating between self and non-self mRNAs (Metz et al.,  
260 2013; Wu et al., 2019).

261

262 *ERAD*. Accumulation of viral proteins during virion assembly at the ER-Golgi interface can trigger  
263 ERAD. Accordingly, we found the ERAD regulator *ERLIN1* to strongly attenuate late stages of SARS-  
264 CoV-2 replication. Two additional factors, *RETREG1* and *FNDC4*, also involved in this pathway with  
265 roles as a ER-phagy receptor and association with the aggresome (Wilkinson, 2019), were also found to  
266 restrict SARS-CoV-2 replication, suggesting that ERAD is a critical cellular antiviral mechanism  
267 triggered during SARS-CoV-2 infection.

268

269 *Vesicle Trafficking*. Trans-Golgi vesicle budding was found as an enriched network for the control of  
270 SARS-CoV-2 replication (**Fig 2C**). Proteins within this network include the heat shock protein *HSPA8*,  
271 and the 2',3'-cyclic nucleotide 3' phosphodiesterase *CNP*; both mapped to late stage viral replication  
272 (**Fig 3C**). *HSPA8* is involved in vesicle uncoating, whereas *CNP* was reported to inhibit release of human  
273 immunodeficiency virus 1 (HIV-1) (Wilson et al., 2012). Notably, these ISGs were found in a protein  
274 complex with *NAPA*, another identified restriction factor for SARS-CoV-2, and a member of the  
275 SNARE complex that functions to dock and fuse vesicles to target membranes. Finally, the GTPase  
276 *Rab27a* also impeded late stages of replication. *Rab27a* controls exocytic transport through fusion of  
277 multivesicular endosomes to the plasma membrane (Ostrowski et al., 2010), further underscoring the  
278 control of vesicular trafficking as a critical antiviral mechanism to control SARS-CoV-2 replication.

279

ER= Endoplasmic Reticulum

#### 280 **BST2 inhibits release of SARS-CoV-2 and is antagonized by Orf7a**

281 The bone marrow stromal antigen 2 (BST2; also known as CD317 or tetherin) was identified as  
282 a potent inhibitor of SARS-CoV-2 replication (**Fig 3C**). BST2 traffics through the ER and Golgi, and  
283 localizes at the plasma membrane and in endosomes. It has been shown to inhibit viral release of several  
284 enveloped viruses, including HIV-1, human coronavirus 229E, and SARS-CoV-1, that either bud at the  
285 plasma membrane or at the ERGIC by tethering their virions to the cell surface or intracellular  
286 membranes (Neil et al., 2008; Taylor et al., 2015; Van Damme et al., 2008; Wang et al., 2014).

287

288 BST2 restriction of SARS-CoV-2 replication was further confirmed in ACE2/TMPRSS2-expressing  
289 293T and Huh7 cells at 24 and 48 h post-infection (**Fig 5A, B, S2A**). We next conducted  
290 loss-of-function studies in HeLa cells, since these harbor constitutive expression of BST2 (Neil et al.,  
291 2008; Van Damme et al., 2008), and found that cells depleted for BST2 released significantly more  
292 infectious viruses over time (**Fig 5C, S2B**). Overall, these data strongly support a role for BST2 in the  
293 restriction of SARS-CoV-2 replication.

294

295 Notably, BST2 expression reduced SARS-CoV-2 RNA replication (53% reduction compared  
296 to control cells) followed by a more potent reduction of viral release (74% reduction) (**Fig 3B, C**). To  
297 further characterize the impact of BST2 on late stage replication, we evaluated viral egress in the  
298 presence or absence of BST2 using a virus-like particle (VLP) system that bypasses viral entry and viral

299 RNA replication (Siu et al., 2008). We confirmed that this system can recapitulate virus egress, as  
300 transfection of viral M, N, and E, but not E and N alone, resulted in secreted N protein (**Fig S2C**). Using  
301 this system, we detected a strong reduction of VLP release in the presence of BST2, evidenced by loss  
302 of secreted N, corroborating that BST2 acts to inhibit egress of SARS-CoV-2 (**Fig 5D**). We next  
303 investigated if BST2 colocalizes with SARS-CoV-2 structural proteins. Notably, we detected  
304 colocalization of BST2 and structural proteins M and S at intracellular foci within the perinuclear region  
305 (caption 2, **Fig 5E, S2D**) but not at the plasma membrane (caption 1, **Fig 5E**). Together, these data  
306 indicate that BST2 spatially associates with SARS-CoV-2 structural proteins during viral assembly and  
307 trafficking.  
308

309 Several viruses have developed evasion strategies to overcome restriction by BST2, including  
310 the HIV-1 accessory protein Vpu and SARS-CoV-1 Orf7a (Neil et al., 2008; Taylor et al., 2015; Van  
311 Damme et al., 2008). Notably, we found that both HIV-1 Vpu and SARS-CoV-2 Orf7a expression  
312 partially rescued BST2-mediated inhibition of SARS-CoV-2 release (**Fig 5D**), and that both Orf7a and  
313 BST2 were incorporated into the VLP particles (**Fig 5D**) (Fitzpatrick et al., 2010). We further  
314 investigated the location of BST2 and Orf7a in the cell and observed that **BST2 and Orf7a colocalized**  
315 **in the perinuclear region (Fig 5F)**. To further investigate Orf7a antagonism of BST2, we infected  
316 parental or BST2 293T stable cells with either WT SARS-CoV-2 or a recombinant SARS-CoV-2 that  
317 was engineered to replace Orf7a with nanoluciferase (dOrf7a) (kindly provided by Ralph Baric) (Hou  
318 et al., 2020). While WT and dOrf7a viruses grew similarly in parental cells, the replication of dOrf7a  
319 virus was significantly attenuated in BST2-expressing cells at 48 h post-infection (**Fig 5G**). Overall,  
320 these data establish BST2 as a potent inhibitor of SARS-CoV-2 egress, and demonstrate that viral Orf7a  
321 protein enables immune evasion through the antagonism of BST2 restriction.  
322

### 323 Comparative antiviral activities of SARS-CoV-2 restriction factors

324 Finally, to understand if discrete cellular defense strategies are deployed to inhibit SARS-CoV-  
325 2 replication, the restriction dataset was cross-referenced with published single ISG overexpression  
326 studies that covered 20 different RNA and DNA viruses, including influenza A virus (FluAV), West  
327 Nile virus (WNV), HCV, and HIV-1 (Schoggins et al., 2011, 2014) (**Fig 6**). Interestingly, ten SARS-  
328 CoV-2 ISGs were found to reduce replication of four or more viruses (**Fig 6**). These include well  
329 described IFN signaling transducers, signaling molecules, and innate immune sensors *STAT2*, and  
330 *MYD88*, inhibitors of viral entry *IFITM2* and *IFITM3* (Brass et al., 2009), and viral nucleic acid binders  
331 *ZBPI* and *IFIT1*. Conversely, a cluster of 8 ISGs harbored selective activities for SARS-CoV-2 (**Fig 6**),  
332 including ER-Golgi resident proteins *NAPA*, *APOL2*, and *ERLIN1*. Notably, significant enrichment in  
333 ISGs that regulate ER homeostasis and Golgi transport suggest that these organelles are critical sites for  
334 the cellular control of SARS-CoV-2 replication. Surprisingly, many of these antiviral factors have not  
335 been reported to impact other viruses that rely on these membranous compartments for replication and

336 assembly, including flavi-, toga-, arteri-, and bunyaviruses, suggesting that these cellular defense  
337 mechanisms target unique aspects of coronavirus translation, assembly, and egress.

338

339 Taken together, this comprehensive analysis of the ISGs that act to impede SARS-CoV-2  
340 revealed that the IFN response to SARS-CoV-2 infection relies on a limited subset of ISGs that govern  
341 a diverse set of cellular functions, including endocytosis, nucleotide biosynthesis and sphingolipid  
342 metabolism. Further dissection of these critical host-pathogen interactions, as well as potential viral  
343 evasion strategies, will enable insights into the molecular determinants of innate immune control of  
344 SARS-CoV-2 replication and clinical disease outcomes.

345

## 346 DATA AVAILABILITY

347

348 The A549 and HTBE RNA-seq data used in this study have been deposited in the Gene Expression  
349 Omnibus (GEO) database repository under the accession number GSE156295 (token  
350 whyhqqupvadjgn).

351

## 352 ACKNOWLEDGMENTS

353

354 We would like to thank Ralph Baric for providing the dOrf7a SARS-CoV-2, Thomas Rogers for  
355 providing the HeLa-ACE2 cells, Kwok-Yung Yuen for providing the rabbit-anti-SARS-CoV-2 N  
356 antibody, and Stefan Pohlmann for providing the mammalian expression vector encoding SARS-CoV-  
357 2 S, pCG1-CoV2-S-HA. We also would like to thank Marisol Chacon for administrative support, Sylvie  
358 Blondelle and Larry Adelman for biosafety support, and Rowland Eaden for shipping assistance. We  
359 would also like to thank the Viral Vector Core Facility at the SBP for the cDNA normalization and the  
360 lentivirus production. This work was supported by the following grants to the Sanford Burnham Prebys  
361 Medical Discovery Institute and the Icahn School of medicine at Mount Sinai: DoD: W81XWH-20-1-  
362 0270; DHIPC: U19 AI118610; Fluomics/NOSI: U19 AI135972. This work was also supported by  
363 generous philanthropic donations from Dinah Ruch and Susan & James Blair, from the JPB Foundation,  
364 the Open Philanthropy Project (research grant 2020-215611 (5384)) and anonymous donors. Additional  
365 support has been provided by DARPA grant HR0011-19-2-0020 and by CRIP (Center for research on  
366 Influenza Pathogenesis), a NIAID-funded Center of Excellence for Influenza Research and Surveillance  
367 (CEIRS, contract # HHSN272201400008C). This work was additionally supported by the following  
368 grants to Northwestern University Feinberg School of Medicine: a CTSA supplement to NCATS: UL1  
369 TR002389; a CTSA supplement to NUCATS with the generous support of the Dixon family: UL1  
370 TR001422; and a Cancer Center supplement: P30 CA060553, and the following grant to JG at UC San  
371 Diego: NIH grant R37AI081668. This work was also supported by a generous grant from the James B.  
372 Pendleton Charitable Trust. The funding sources had no role in the study design, data collection,

373 analysis, interpretation, or writing of the report. The content of this study is solely the responsibility of  
374 the authors and does not necessarily represent the official views of the National Institutes of Health.  
375

## 376 AUTHOR CONTRIBUTIONS

377 L.M.-S., M.K.L., C.A.S., J.G. and S.K.C., conceived and designed the experiments. L.M.-S., M.K.L.,  
378 X.Y., C.A.S., A.P.G., P.D.J., C.N., Y.P., and A.L.O., conducted and/or analyzed the experiments. L.P.  
379 and A.M.O. conducted data analysis and representation. A.R.F., M.U., M.C. and C.B. performed and/or  
380 analyzed the RNAseq experiments. D.P., C.C., S.L., B.R., and T.I. generated the network model. L.M.  
381 and J.F.H. generated essential reagents. L.M.-S., and S.K.C. wrote the manuscript with contributions  
382 from all authors. Funding Acquisition, L.P., C.B., A.G.-S., and S.K.C.

383

## 384 DECLARATION OF INTERESTS

385 The authors declare no competing interests.

386

## 387 REFERENCES

388 Arunachalam, P.S., Wimmers, F., Mok, C.K.P., Perera, R.A.P.M., Scott, M., Hagan, T., Sigal, N.,  
389 Feng, Y., Bristow, L., Tak-Yin Tsang, O., et al. (2020). Systems biological assessment of immunity to  
390 mild versus severe COVID-19 infection in humans. *Science* eabc6261.

391 Blanco-Melo, D., Nilsson-Payant, B.E., Liu, W.-C., Uhl, S., Hoagland, D., Møller, R., Jordan, T.X.,  
392 Oishi, K., Panis, M., Sachs, D., et al. (2020). Imbalanced Host Response to SARS-CoV-2 Drives  
393 Development of COVID-19. *Cell* 181, 1036-1045.e9.

394 Brass, A.L., Huang, I.-C., Benita, Y., John, S.P., Krishnan, M.N., Feeley, E.M., Ryan, B.J., Weyer,  
395 J.L., van der Weyden, L., Fikrig, E., et al. (2009). The IFITM Proteins Mediate Cellular Resistance to  
396 Influenza A H1N1 Virus, West Nile Virus, and Dengue Virus. *Cell* 139, 1243–1254.

397 Carlin, D.E., Demchak, B., Pratt, D., Sage, E., and Ideker, T. (2017). Network propagation in the  
398 cytoscape cyberinfrastructure. *PLOS Comput. Biol.* 13, e1005598.

399 Dong, E., Du, H., and Gardner, L. (2020). An interactive web-based dashboard to track COVID-19 in  
400 real time. *Lancet Infect. Dis.* S1473309920301201.

401 Emanuel, W., Kirstin, M., Vedran, F., Asija, D., Theresa, G.L., Roberto, A., Filippou, K., David, K.,  
402 Salah, A., Christopher, B., et al. (2020). Bulk and single-cell gene expression profiling of SARS-CoV-  
403 2 infected human cell lines identifies molecular targets for therapeutic intervention. *BioRxiv*  
404 2020.05.05.079194.

405 Fehr, A.R., and Perlman, S. (2015). Coronaviruses: an overview of their replication and pathogenesis.  
406 *Methods Mol. Biol.* Clifton NJ 1282, 1–23.

407 Fitzpatrick, K., Skasko, M., Deerinck, T.J., Crum, J., Ellisman, M.H., and Guatelli, J. (2010). Direct  
408 Restriction of Virus Release and Incorporation of the Interferon-Induced Protein BST-2 into HIV-1  
409 Particles. *PLOS Pathog.* 6, e1000701.

410 García-Sastre, A. (2017). Ten Strategies of Interferon Evasion by Viruses. *Cell Host Microbe* 22, 176–  
411 184.

- 412 Gordon, D.E., Jang, G.M., Bouhaddou, M., Xu, J., Obernier, K., O'Meara, M.J., Guo, J.Z., Swaney,  
413 D.L., Tummino, T.A., Hüttenhain, R., et al. (2020). A SARS-CoV-2-Human Protein-Protein  
414 Interaction Map Reveals Drug Targets and Potential Drug-Repurposing (Systems Biology).
- 415 Hadjadj, J., Yatim, N., Barnabei, L., Corneau, A., Boussier, J., Smith, N., Péré, H., Charbit, B.,  
416 Bondet, V., Chenevier-Gobeaux, C., et al. (2020). Impaired type I interferon activity and inflammatory  
417 responses in severe COVID-19 patients. *Science* eabc6027.
- 418 Hoffmann, M., Kleine-Weber, H., Schroeder, S., Krüger, N., Herrler, T., Erichsen, S., Schiergens,  
419 T.S., Herrler, G., Wu, N.-H., Nitsche, A., et al. (2020). SARS-CoV-2 Cell Entry Depends on ACE2  
420 and TMPRSS2 and Is Blocked by a Clinically Proven Protease Inhibitor. *Cell* 181, 271-280.e8.
- 421 Hou, Y.J., Okuda, K., Edwards, C.E., Martinez, D.R., Asakura, T., Dinnon, K.H., Kato, T., Lee, R.E.,  
422 Yount, B.L., Mascenik, T.M., et al. (2020). SARS-CoV-2 Reverse Genetics Reveals a Variable  
423 Infection Gradient in the Respiratory Tract. *Cell* 182, 429-446.e14.
- 424 Huang, C., Wang, Y., Li, X., Ren, L., Zhao, J., Hu, Y., Zhang, L., Fan, G., Xu, J., Gu, X., et al. (2020).  
425 Clinical features of patients infected with 2019 novel coronavirus in Wuhan, China. *Lancet Lond.  
426 Engl.* 395, 497–506.
- 427 Hubel, P., Urban, C., Bergant, V., Schneider, W.M., Knauer, B., Stukalov, A., Scaturro, P., Mann, A.,  
428 Brunotte, L., Hoffmann, H.H., et al. (2019). A protein-interaction network of interferon-stimulated  
429 genes extends the innate immune system landscape. *Nat. Immunol.* 20, 493–502.
- 430 Hultquist, J.F., Hiatt, J., Schumann, K., McGregor, M.J., Roth, T.L., Haas, P., Doudna, J.A., Marson,  
431 A., and Krogan, N.J. (2019). CRISPR-Cas9 genome engineering of primary CD4+ T cells for the  
432 interrogation of HIV-host factor interactions. *Nat. Protoc.* 14, 1–27.
- 433 Hung, I.F.-N., Lung, K.-C., Tso, E.Y.-K., Liu, R., Chung, T.W.-H., Chu, M.-Y., Ng, Y.-Y., Lo, J.,  
434 Chan, J., Tam, A.R., et al. (2020). Triple combination of interferon beta-1b, lopinavir-ritonavir, and  
435 ribavirin in the treatment of patients admitted to hospital with COVID-19: an open-label, randomised,  
436 phase 2 trial. *Lancet Lond. Engl.* 395, 1695–1704.
- 437 Lamers, M.M., Beumer, J., van der Vaart, J., Knoops, K., Puschhof, J., Breugem, T.I., Ravelli, R.B.G.,  
438 Paul van Schayck, J., Mykytyn, A.Z., Duimel, H.Q., et al. (2020). SARS-CoV-2 productively infects  
439 human gut enterocytes. *Science* 369, 50–54.
- 440 van der Made, C.I., Simons, A., Schuurs-Hoeijmakers, J., van den Heuvel, G., Mantere, T., Kersten,  
441 S., van Deuren, R.C., Steehouwer, M., van Reijmersdal, S.V., Jaeger, M., et al. (2020). Presence of  
442 Genetic Variants Among Young Men With Severe COVID-19. *JAMA*.
- 443 Mathew, D., Giles, J.R., Baxter, A.E., Oldridge, D.A., Greenplate, A.R., Wu, J.E., Alanio, C., Kuri-  
444 Cervantes, L., Pampena, M.B., D'Andrea, K., et al. (2020). Deep immune profiling of COVID-19  
445 patients reveals distinct immunotypes with therapeutic implications. *Science* eabc8511.
- 446 Metz, P., Reuter, A., Bender, S., and Bartenschlager, R. (2013). Interferon-stimulated genes and their  
447 role in controlling hepatitis C virus. *J. Hepatol.* 59, 1331–1341.
- 448 Miller, C.L. (2011). Stress Granules and Virus Replication. *Future Virol.* 6, 1329–1338.
- 449 Nanda, S.K., Johnson, R.F., Liu, Q., and Leibowitz, J.L. (2003). Mitochondrial HSP70, HSP40, and  
450 HSP60 bind to the 3' untranslated region of the Murine hepatitis virus genome. *Arch. Virol.* 149, 93–  
451 111.
- 452 Neil, S.J.D., Zang, T., and Bieniasz, P.D. (2008). Tetherin inhibits retrovirus release and is  
453 antagonized by HIV-1 Vpu. *Nature* 451, 425–430.

- 454 Ostrowski, M., Carmo, N.B., Krumeich, S., Fanget, I., Raposo, G., Savina, A., Moita, C.F., Schauer,  
455 K., Hume, A.N., Freitas, R.P., et al. (2010). Rab27a and Rab27b control different steps of the exosome  
456 secretion pathway. *Nat. Cell Biol.* *12*, 19–30.
- 457 Overmyer, K.A., Shishkova, E., Miller, I., Balnis, J., Bernstein, M.N., Peters-Clarke, T.M., Meyer,  
458 J.G., Quan, Q., Muehlbauer, L.K., Trujillo, E.A., et al. (2020). Large-scale Multi-omic Analysis of  
459 COVID-19 Severity (Infectious Diseases (except HIV/AIDS)).
- 460 Pfaender, S., Mar, K.B., Michailidis, E., Kratzel, A., Boys, I.N., V'kovski, P., Fan, W., Kelly, J.N.,  
461 Hirt, D., Ebert, N., et al. (2020). LY6E impairs coronavirus fusion and confers immune control of viral  
462 disease. *Nat. Microbiol.* *1*–10.
- 463 Raudvere, U., Kolberg, L., Kuzmin, I., Arak, T., Adler, P., Peterson, H., and Vilo, J. (2019).  
464 g:Profiler: a web server for functional enrichment analysis and conversions of gene lists (2019  
465 update). *Nucleic Acids Res.* *47*, W191–W198.
- 466 Rosenzweig, R., Nillegoda, N.B., Mayer, M.P., and Bukau, B. (2019). The Hsp70 chaperone network.  
467 *Nat. Rev. Mol. Cell Biol.* *20*, 665–680.
- 468 Schoggins, J.W., Wilson, S.J., Panis, M., Murphy, M.Y., Jones, C.T., Bieniasz, P., and Rice, C.M.  
469 (2011). A diverse range of gene products are effectors of the type I interferon antiviral response.  
470 *Nature* *472*, 481–485.
- 471 Schoggins, J.W., MacDuff, D.A., Imanaka, N., Gainey, M.D., Shrestha, B., Eitson, J.L., Mar, K.B.,  
472 Richardson, R.B., Ratushny, A.V., Litvak, V., et al. (2014). Pan-viral specificity of IFN-induced genes  
473 reveals new roles for cGAS in innate immunity. *Nature* *505*, 691–695.
- 474 Seifert, L.L., Si, C., Saha, D., Sadic, M., Vries, M. de, Ballentine, S., Briley, A., Wang, G., Valero-  
475 Jimenez, A.M., Mohamed, A., et al. (2019). The ETS transcription factor ELF1 regulates a broadly  
476 antiviral program distinct from the type I interferon response. *PLOS Pathog.* *15*, e1007634.
- 477 Shannon, P. (2003). Cytoscape: A Software Environment for Integrated Models of Biomolecular  
478 Interaction Networks. *Genome Res.* *13*, 2498–2504.
- 479 Siu, Y.L., Teoh, K.T., Lo, J., Chan, C.M., Kien, F., Escriou, N., Tsao, S.W., Nicholls, J.M., Altmeyer,  
480 R., Peiris, J.S.M., et al. (2008). The M, E, and N Structural Proteins of the Severe Acute Respiratory  
481 Syndrome Coronavirus Are Required for Efficient Assembly, Trafficking, and Release of Virus-Like  
482 Particles. *J. Virol.* *82*, 11318–11330.
- 483 Spinnenhirn, V., Farhan, H., Basler, M., Aichem, A., Canaan, A., and Groettrup, M. (2014). The  
484 ubiquitin-like modifier FAT10 decorates autophagy-targeted Salmonella and contributes to Salmonella  
485 resistance in mice. *J. Cell Sci.* *127*, 4883–4893.
- 486 Sun, J., Ye, F., Wu, A., Yang, R., Pan, M., Sheng, J., Zhu, W., Mao, L., Wang, M., Huang, B., et al.  
487 (2020). Comparative transcriptome analysis reveals the intensive early-stage responses of host cells to  
488 SARS-CoV-2 infection. *BioRxiv* *2020.04.30.071274*.
- 489 Taylor, J.K., Coleman, C.M., Postel, S., Sisk, J.M., Bernbaum, J.G., Venkataraman, T., Sundberg,  
490 E.J., and Frieman, M.B. (2015). Severe Acute Respiratory Syndrome Coronavirus ORF7a Inhibits  
491 Bone Marrow Stromal Antigen 2 Virion Tethering through a Novel Mechanism of Glycosylation  
492 Interference. *J. Virol.* *89*, 11820–11833.
- 493 Van Damme, N., Goff, D., Katsura, C., Jorgenson, R.L., Mitchell, R., Johnson, M.C., Stephens, E.B.,  
494 and Guatelli, J. (2008). The interferon-induced protein BST-2 restricts HIV-1 release and is  
495 downregulated from the cell surface by the viral Vpu protein. *Cell Host Microbe* *3*, 245–252.

- 496 Wang, S.-M., Huang, K.-J., and Wang, C.-T. (2014). BST2/CD317 counteracts human coronavirus  
497 229E productive infection by tethering virions at the cell surface. *Virology* *449*, 287–296.
- 498 Whitt, M.A. (2010). Generation of VSV pseudotypes using recombinant ΔG-VSV for studies on virus  
499 entry, identification of entry inhibitors, and immune responses to vaccines. *J. Virol. Methods* *169*,  
500 365–374.
- 501 Wilkinson, S. (2019). ER-phagy: shaping up and destressing the endoplasmic reticulum. *FEBS J.* *286*,  
502 2645–2663.
- 503 Wilson, G.J., Marakalala, M.J., Hoving, J.C., van Laarhoven, A., Drummond, R.A., Kerscher, B.,  
504 Keeton, R., van de Vosse, E., Ottenhoff, T.H.M., Plantinga, T.S., et al. (2015). The C-type lectin  
505 receptor CLECSF8/CLEC4D is a key component of anti-mycobacterial immunity. *Cell Host Microbe*  
506 *17*, 252–259.
- 507 Wilson, S.J., Schoggins, J.W., Zang, T., Kutluay, S.B., Jouvenet, N., Alim, M.A., Bitzegeio, J., Rice,  
508 C.M., and Bieniasz, P.D. (2012). Inhibition of HIV-1 Particle Assembly by 2',3'-Cyclic-Nucleotide 3'-  
509 Phosphodiesterase. *Cell Host Microbe* *12*, 585–597.
- 510 Wu, N., Nguyen, X.-N., Wang, L., Appourchaux, R., Zhang, C., Panthu, B., Gruffat, H., Journo, C.,  
511 Alais, S., Qin, J., et al. (2019). The interferon stimulated gene 20 protein (ISG20) is an innate defense  
512 antiviral factor that discriminates self versus non-self translation. *PLOS Pathog.* *15*, e1008093.
- 513 Zang, R., Case, J.B., Castro, M.F.G., Liu, Z., Zeng, Q., Zhao, H., Son, J., Rothlauf, P.W., Hou, G.,  
514 Bose, S., et al. (2020). Cholesterol 25-hydroxylase suppresses SARS-CoV-2 replication by blocking  
515 membrane fusion. *BioRxiv* 2020.06.08.141077.
- 516 Zhang, T., Yin, C., Boyd, D.F., Quarato, G., Ingram, J.P., Shubina, M., Ragan, K.B., Ishizuka, T.,  
517 Crawford, J.C., Tummers, B., et al. (2020). Influenza Virus Z-RNAs Induce ZBP1-Mediated  
518 Necroptosis. *Cell* *180*, 1115-1129.e13.
- 519 Zhu, C.-H., Kim, J., Shay, J.W., and Wright, W.E. (2008). SGNP: an essential Stress  
520 Granule/Nucleolar Protein potentially involved in 5.8s rRNA processing/transport. *PloS One* *3*, e3716.
- 521
- 522 **METHODS**
- 523

524 **Cells and Viruses.** SARS-CoV-2 USA-WA1/2020, isolated from an oropharyngeal swab from a patient  
525 with a respiratory illness who developed clinical disease (COVID-19) in January 2020 in Washington,  
526 USA, was obtained from BEI Resources (NR-52281). The recombinant dOrf7a SARS-CoV-2 was  
527 kindly provided by Ralph Baric (Hou et al., 2020). These viruses were propagated using Vero E6 cells,  
528 collected after one passage, aliquoted, and stored at -80 °C. Plaque forming unit (PFU) assays were  
529 performed to titrate the cultured virus. All experiments involving live SARS-CoV-2 followed the  
530 approved standard operating procedures of the Biosafety Level 3 facility at the Sanford Burnham Prebys  
531 Medical Discovery Institute. Vero E6 (ATCC CRL-1586), HEK293T (ATCC CRL-3216), HeLa (ATCC  
532 CRL-1586), and Huh7 (Apath LLC, Brooklyn) cells were maintained in cell growth media: Dulbecco's  
533 modified eagle medium (DMEM, Gibco) supplemented with 10 % heat-inactivated fetal bovine serum  
534 (FBS, Gibco), 50 U/mL penicillin - 50 µg/mL streptomycin (Fisher Scientific), 1 mM sodium pyruvate  
535 (Gibco), 10 mM 4-(2-hydroxyethyl)-1-piperazineethanesulfonic acid (HEPES, Gibco), and 1X MEM

536 non-essential amino acids solution (Gibco). BHK-21/WI-2 cells (Kerafast, MA) were maintained in  
537 DMEM (Gibco) supplemented with 10 % heat-inactivated FBS (Gibco) and 50 U/mL penicillin -  
538 50 µg/mL streptomycin. Human tracheobronchial epithelial (HTBE) cells (ATCC PCS-300-010) were  
539 cultured in commercially available airway epithelial cell basal medium following manufacturer's  
540 protocol (ATCC). HTBE cells were derived from one donor and all tissues used for isolation of these  
541 cells were obtained under informed consent and conform to HIPAA standards to protect the privacy of  
542 the donors' personal health information. HEK293T and HeLa cells stably expressing ACE2 (293T-  
543 ACE2/HeLa-ACE2) were generated by transducing HEK293T or HeLa cells with human ACE2-  
544 expressing lentiviruses, followed by selection of resistant cells with puromycin (InvivoGen) at 2 µg/ml  
545 for 14 days. The resistant cells were then maintained in cell growth media supplemented with 1 µg/ml  
546 puromycin. ACE2 expression was confirmed by western blot analysis. All cells were tested and were  
547 confirmed to be free of mycoplasma contamination.

548

549 **Antibodies.** The antibodies used in this study include: *Immunofluorescence*: rabbit anti-SARS-CoV-2  
550 N antibody (gift from Kwok-Yung Yuen, University of Hong Kong), mouse anti-HM1.24 (BST2) (a  
551 gift from Chugai Pharmaceutical Co., Kanagawa, Japan), rat anti-FLAG-AlexaFluor-488 (Biolegend,  
552 #637317), mouse anti-HA-AlexaFluor-594 (Biolegend, #901511), donkey anti-mouse-AlexaFluor-488  
553 (Jackson ImmunoResearch, #715-545-150), donkey anti-mouse-Rhodamine-Red-X (Jackson  
554 ImmunoResearch, #715-295-150). *Western blotting*: rabbit polyclonal anti-BST2 (NIH AIDS Reagent  
555 Program, Division of AIDS, NIAID, NIH: Anti-BST-2 Polyclonal (cat# 11721) from Drs. Klaus Strebel  
556 and Amy Andrew), mouse monoclonal anti-V5 tag (Invitrogen, #R960-25), mouse monoclonal anti-  
557 GAPDH (GeneTex, #GTX627408), mouse monoclonal anti-FLAG M2 (Sigma, #F1804), rabbit  
558 monoclonal anti-β-actin antibody (Cell Signaling, #4970) and rabbit monoclonal anti-CoxIV antibody  
559 (Cell Signaling #4850).

560

561 **Plasmids.** *Lentiviral constructs*: pLX304 constructs for each of the ISGs, and GFP and CAT as negative  
562 controls were obtained from the ORFeome library. psPAX2 (Addgene, #12260), and pMD2.G  
563 (Addgene, #12259). *SARS-CoV-2 constructs*: dsDNA gene fragments (gBlocks) encoding human-codon-  
564 optimized SARS-CoV-2 proteins M, M-FLAG, E, E-V5, N, N-V5, and Orf7a N- or C-terminally tagged  
565 with 3xFLAG tag, corresponding to the SARS-CoV-2 Wuhan-Hu-1 isolate (genbank MN908947.3),  
566 were synthesized by Integrated DNA Technologies (IDT). The gene fragments were inserted into the  
567 pcDNA3.1(-) backbone between NotI and EcoRI restriction sites using an In-fusion seamless cloning  
568 strategy (Takara Bio). The mammalian expression vector encoding COV2 S, pCG1-COV2-S-HA, was  
569 obtained from Prof. Stefan Pohlmann (Infection Biology Unit, German Primate Center - Leibniz  
570 Institute for Primate Research, University Göttingen (Hoffmann et al., 2020)).

571

572 **RNA-seq experiments.** HTBE and A549 cells were seeded overnight and then treated with 100 IU/ml  
573 universal interferon beta (IFN, R&D Systems), or left untreated. At 8 h post-treatment, cell were lysed  
574 in Trizol (Thermo Fisher) and RNA was extracted using RNeasy Mini Kit (Qiagen). Strand-specific  
575 ribosomal RNA-depleted sequencing libraries were produced according to standard Illumina protocols,  
576 and sequencing was carried out on an Illumina HiSeq 2500. The human hg38 reference genome and  
577 RefSeq gene annotation were used for spliced read alignment and gene assignment. Experiments were  
578 conducted in duplicate and 412 genes were defined as ISGs based on log2FC > 1.5 and p value < 0.05.  
579

580 **Overexpression cDNA screen.** A targeted overexpression cDNA screen was carried out in human  
581 epithelial cells to identify ISGs that restrict the replication of SARS-CoV-2. 399 ISGs were selected for  
582 this gain-of-function screen based on experimental, published data, and availability as full-length,  
583 sequence-validated cDNA clones. These cDNAs were hand-picked from the ORFeome collection,  
584 which contains ~17,000 full-length, sequenced, V5-epitope tagged human ORFs in the lentiviral  
585 expression vector pLX304. Each of these 399 cDNAs were individually arrayed in 384-well plates at a  
586 concentration of 40ng/well along with human ACE2 and TMPRSS2 (10 ng), and 0.25 µl of the  
587 transfection reagent Fugene 6 (Promega). After 20 min incubation at room temperature, 3,000 293T  
588 cells diluted in cell growth media (see *cells and viruses* section) were seeded per well and incubated at  
589 37°C, 5% CO<sub>2</sub>. At 30 h post-transfection, cells were mock-treated or infected with SARS-CoV-2 (USA-  
590 WA1/2020) at a MOI 0.0625 for 40 h at 37°C, 5% CO<sub>2</sub>. Cells were then fixed with 5% PFA (Boston  
591 BioProducts) for 4 hours at room temperature and then washed twice with 1xPBS. Cells were  
592 permeabilized with 0.5% Triton X-100 for 20 min, followed by two washes with 1xPBS and blocking  
593 with 3% BSA (Sigma) for 1 h at room temperature. Anti-SARS-CoV-2 N rabbit serum was added for 1  
594 h at room temperature, followed by three washes with 1xPBS and a 1-h incubation with Alexa Fluor  
595 568-conjugated anti-rabbit secondary antibody (Thermo Fisher Scientific) diluted in 3% BSA.  
596 Following three washes with PBS, cells were stained with DAPI (4,6-diamidino-2-phenylindole, KPL),  
597 and plates were sealed and stored at 4°C until imaging.  
598

599 **High-content imaging and data analysis.** Viral replication was assessed using high-throughput  
600 microscopy. The assay plates were imaged using the IC200 imaging system (Vala Sciences) located at  
601 the Conrad Prebys Center for Chemical Genomics (CPCCG). The analysis software Columbus v2.5  
602 (Perkin Elmer) was used to calculate infectivity (number Alexa 568+ objects/number DAPI+ objects).  
603 Screens were run in duplicate and the infectivity values for each well were normalized to the median of  
604 the negative control CAT, and used to calculate the log2FC. The hit calling strategy was based on  
605 log2FC. Factors with a corresponding log2FC < 4\*Stdev CAT , and cell viability > 70 % CAT were  
606 considered restriction factors.  
607

608 **Generation lentivirus and 293T-ACE2-ISG/GFP cells.** Lentiviruses were generated for each of the  
609 65 ISGs that were found to restrict SARS-CoV-2 replication. Briefly, 293T cells at passage 10 were  
610 cultured in monolayer on matrigel-coated plates. After reaching 90% of density, three plasmids,  
611 including pLX304-ISG/GFP, psPAX2 (Addgene), and pMD2.G (Addgene), were co-transfected into  
612 cells at a ratio of 3:2:1 using PEI (VWR). After 16 h incubation, transfection media were replaced with  
613 fresh DMEM supplemented with 10% FBS. Viral supernatants were collected at 48 h post-transfection  
614 with an estimated transduction unit of  $2 \times 10^4$  lentiviral particles. Lentiviruses were used to transduce  
615 293T-ACE2 cells (MOI = 3) pre-treated with 10 µg/ml Polybrene (Life Technologies), followed by  
616 selection of resistant cells with Blasticidin (InvivoGen) at 10 µg/ml for 14 days. 293T-ACE2-ISG/GFP  
617 resistant cells were maintained in cell growth media supplemented with 2 µg/ml Blasticidin.  
618

619 **Network analyses.** To understand the biochemical and functional context by which the identified  
620 antiviral ISGs function, we explored a network-based approach that could integrate these ISGs (“seed”  
621 proteins) with existing knowledge. Towards this aim, we used a pipeline that employs a combination of  
622 scripts and Cytoscape applications. First, to explore the highest confidence interactions of “seed”  
623 proteins, we selected the STRING - Human Protein Links - High Confidence (Score  $\geq 0.7$ ) protein-  
624 protein interaction network available on NDEx as the “background” network (link provided below). We  
625 then performed network propagation to select a neighborhood of 343 proteins ranked highest by the  
626 algorithm with respect to these seeds (Carlin et al., 2017). This “neighborhood” network (including all  
627 edges among the 343 proteins) was extracted from the background network. We then identified densely  
628 interconnected regions, i.e. “communities” within the neighborhood network, using the community  
629 detection algorithm HiDef via the Community Detection Application and Service (CDAPS)  
630 (manuscript in press, app available at <http://apps.cytoscape.org/apps/cycommunitydetection>). The result  
631 of HiDef from CDAPS was a “hierarchy” network where each node represented a community of  
632 proteins, and edges denoted containment of one community (the “child”) by another (the “parent”).  
633 Finally, the hierarchy network was styled, communities were labeled by functional enrichment using  
634 gProfiler (via CDAPS) and a layout was applied. The STRING - Human Protein Links - High  
635 Confidence (Score  $>= 0.7$ ) network is available in the Network Data Exchange (NDEx) at  
636 <http://ndexbio.org/#/network/275bd84e-3d18-11e8-a935-0ac135e8bacf>.  
637

638 **Generation pseudotyped SARS-CoV-2 virus.** VSV pseudotyped with spike (S) protein of SARS-  
639 CoV-2 was generated according to a published protocol (Whitt, 2010). Briefly, BHK-21/WI-2 cells  
640 (Kerafast, MA) transfected with SARS-CoV-2 S protein were inoculated with VSV-G pseudotyped ΔG-  
641 luciferase VSV (Kerafast, MA). After a 2 hour incubation at 37 °C, the inoculum was removed and cells  
642 were treated with DMEM supplemented with 5 % FBS, 50 U/mL penicillin, and 50 µg/mL  
643 streptomycin. Pseudotyped particles were collected 24 h post-inoculation, then centrifuged at 1,320×g  
644 to remove cell debris and stored at –80 °C until use.

645

646 **Mapping into SARS-CoV-2 infectious cycle studies.** Mapping studies were conducted in parallel  
647 using 293T-ACE2-ISG/GFP cells. Briefly, multiple 96-well plates were seeded with 50,000 293T-  
648 ACE2-ISG/GFP cells/well and incubated overnight at 37°C, 5% CO<sub>2</sub>. To determine the effect of the  
649 identified ISGs on *viral entry*, 293T-ACE2-ISG/GFP cells were infected with VSV-S-luciferase and  
650 incubated for 16 h. The activity of firefly luciferase was then measured using the bright-Glo™ luciferase  
651 assay (Promega) for quantitative determination. To measure *RNA replication* and *late stages*, cells were  
652 infected with SARS-CoV-2 (USA-WA1/2020) at a MOI 4 for 1 h on ice. Viral inoculum was removed  
653 and cells were washed twice with 1xPBS and supplemented with cell growth media (see *cells and viruses*  
654 section). At 6 h post-infection, SARS-CoV-2 *RNA replication* was measured. Briefly, intracellular viral  
655 RNA was purified from infected cells using the TurboCapture mRNA Kit (Qiagen) in accordance with  
656 the manufacturer's instructions. The purified RNA was subjected to first-strand cDNA synthesis using  
657 the high-capacity cDNA reverse transcription kit (Applied Biosystems, Inc). Real-time quantitative PCR  
658 (RT-qPCR) analysis was then performed using TaqPath one-step RT-qPCR Master Mix (Applied  
659 Biosystems, Inc) and, ActinB CTRL Mix (Applied Biosystems, Inc) for housekeeping genes, and the  
660 following primers and probe for qPCR measurements of viral genes: N-Fwd: 5'-  
661 TTACAAACATTGGCCGCAAA-3'; N-Rev: 5'-GCGCGACATTCCGAAGAA-3'; N-Probe: 5'-  
662 FAM-ACAATTGCCCGAGCGCTTCAG-BHQ-3'. To evaluate *late stages*, supernatants collected  
663 at 18 h post-infection were used to infect naïve Vero E6 cells. At 18 h post-infection cells were then  
664 fixed with 5% PFA (Boston BioProducts) for 4 hours at room temperature and then subjected to  
665 immunostaining and imaging for SARS-CoV-2 N protein and DAPI (described in *overexpression cDNA*  
666 *screen* section).

667

668 **Generation of CRISPR-Cas9 BST2 KO HeLa-ACE2 cells.** Detailed protocols for RNP production  
669 have been previously published (Hultquist et al., 2019). Briefly, lyophilized guide RNA (gRNA) and  
670 tracrRNA (Dharmacon) were suspended at a concentration of 160 μM in 10 mM Tris-HCL, 150mM  
671 KCl, pH 7.4. 5μL of 160μM gRNA was mixed with 5μL of 160μM tracrRNA and incubated for 30 min  
672 at 37°C. The gRNA:tracrRNA complexes were then mixed gently with 10μL of 40μM Cas9 (UC-  
673 Berkeley Macrolab) to form CRISPR-Cas9 ribonucleoproteins (crRNPs). Five 3.5μL aliquots were  
674 frozen in Lo-Bind 96-well V-bottom plates (E&K Scientific) at -80°C until use. BST2 gene was targeted  
675 by 5 pooled gRNA derived from the Dharmacon pre-designed Edit-R library for gene knock-out. *BST2*  
676 (g1:TGCATCCAGGGAAAGCCATTA, CM-011817-01; g2:TTGGGCCTCTGCATCCA, CM-  
677 011817-02; g3:TTGAGGAGCTTACCAAGTG, CM-011817-03; g4:  
678 TCACTGCCGAAGGCCGTCC, CM-011817-04; g5: CACCATCAAGGCCAACAGCG, CM-  
679 011817-05). Non-targeting negative control gRNA (Dharmacon, U-007501) was delivered in parallel.  
680 Each electroporation reaction consisted of 2.5x10<sup>5</sup> HeLa-ACE2 cells, 3.5 μL crRNPs, and 20 μL  
681 electroporation buffer. HeLa-ACE2 cells were grown in fully supplemented MEM (10% FBS,

682 1xPen/Strep, 1x non-essential amino acids) to 70% confluency, suspended and counted. crRNPs were  
683 thawed and allowed to come to room-temperature. Immediately prior to electroporation, cells were  
684 centrifuged at 400xg for 3 minutes, supernatant was removed by aspiration, and the pellet was  
685 resuspended in 20 µL of room-temperature SE electroporation buffer plus supplement (Lonza) per  
686 reaction. 20 µL of cell suspension was then gently mixed with each crRNP and aliquoted into a 96-well  
687 electroporation cuvette for nucleofection with the 4-D Nucleofector X-Unit (Lonza) using pulse code  
688 EO-120. Immediately after electroporation, 80 µL of pre-warmed media was added to each well and  
689 cells were allowed to rest for 30 minutes in a 37°C cell culture incubator. Cells were subsequently moved  
690 to 12-well flat-bottomed culture plates pre-filled with 500 µL pre-warmed media. Cells were cultured  
691 at 37°C / 5% CO<sub>2</sub> in a dark, humidified cell culture incubator for 4 days to allow for gene knock-out  
692 and protein clearance prior to downstream applications.

693

694 **SARS-CoV-2 viral growth assays.** To evaluate SARS-CoV-2 viral growth, the amount of released  
695 infectious particles was measured by plaque assay. Briefly, supernatants from SARS-CoV-2 infected  
696 cells were collected at indicated time points and stored at -80°C until used. 600,000 Vero E6 cells were  
697 seeded and incubated overnight at 37°C / 5% CO<sub>2</sub> in 12-well plates. Confluent Vero E6 cells were then  
698 washed once with 1xPBS and infected with 100µl of virus-containing supernatants that were serially  
699 diluted 1:10. Plates were incubated 1 h at room temperature, followed by inoculum removal and addition  
700 of 1ml overlay media (2xMEM and 2.5% Avicel (FMC BioPolymer, RC-591 NF) at 1:1 ratio). 2xMEM  
701 contains 100 ml 10x MEM (Gibco), 10 ml 100x penicillin-streptomycin (Fisher Scientific), 10 ml 100x  
702 L-Glutamine, 6 ml 35% BSA, 10 ml 10 mM 4-(2-hydroxyethyl)-1-piperazineethanesulfonic acid  
703 (HEPES, Gibco), 24 mL 5% NaHCO<sub>3</sub> (Gibco) and 340 ml water. Plates were incubated 3 days at 37°C,  
704 5%CO<sub>2</sub>, and then fixed and stained using 0.1% Crystal Violet and 5% PFA (Boston BioProducts)  
705 overnight at 4°C.

706

707 **VLP assays.** HEK-293T cells seeded in 6-well plates were transfected using Lipofectamine 2000  
708 (Thermo-Fisher) with 625 ng each of plasmids encoding M-FLAG, E-V5, N-V5 (Fig 5D), or 500 ng of  
709 M, E, and N-V5 (Fig S2C), with or without 625 ng 3xFLAG-Orf7a or human codon-optimized HIV-  
710 1 Vpu (pVpHu from Klaus Strebler) with or without 75 ng BST2 (pcDNA3.1-BST-2 from Autumn Ruiz  
711 and Edward Stephens). After 24 hours, supernatants were collected and clarified of cell debris then  
712 pelleted through 20% sucrose at 23,500 x g for 1 hr at 4°C. Pelleted VLPs and cells were lysed in 2X  
713 Laemmli SDS-PAGE buffer, then run on 12% SDS-PAGE gels, transferred to PVDF membranes and  
714 blotted with the indicated antibodies.

715

716 **Colocalization studies. Immunofluorescence Staining:** 2x10<sup>4</sup> HeLa-ACE2 cells were seeded on 12 mm  
717 glass coverslips in 24-well plates, 24 h prior to transfection. The cells were transfected with 800 ng total  
718 plasmid DNA, using Lipofectamine 2000 (Thermo-Fisher), diluted in Optimem, according to

719 manufacturer's instructions. HeLa-ACE2 cells were either transfected with equal amounts (200 ng) of  
720 SARS-CoV-2 structural proteins M, E, N, S-HA, or M-FLAG, E, N, and empty plasmid (pcDNA3.1).  
721 HeLa-ACE2 cells were also transfected with 800 ng ORF7a-3xFLAG. 24 h post-transfection, cells were  
722 washed briefly in 4°C PBS before incubation with ice-cold 4% paraformaldehyde (PFA, diluted in PBS,  
723 pH 7.4). The PFA was allowed to warm to RT as the cells were fixed for 20 minutes, the PFA was  
724 removed and cells washed 3x in 1XPBS (5 min per wash). The fixed cells were quenched with 50 mM  
725 Ammonium chloride (in PBS) for 5 minutes RT, washed 3 x in PBS, and permeabilized with 0.2%  
726 Triton X-100 for 7 minutes (RT). The cells were again washed in three times in 1X PBS before  
727 incubation with 2% bovine serum albumin (BSA) in PBS for 30 minutes, prior to incubation with  
728 primary antibodies overnight at 4°C. Cells transfected with M, E, N and S-HA were stained overnight  
729 with mouse anti-HM1.24 (BST-2) antibody (diluted 1:300 in 1% BSA in PBS) at 4°C. The following  
730 day, the cells were washed 3x PBS and incubated with donkey anti-mouse-AlexaFluor-488 (1:400) for  
731 2hr RT. The cells were washed 3x PBS (10 min per wash) and blocked with 2% BSA in PBS  
732 supplemented with 5% normal mouse serum for 1 hr RT, briefly washed in 2% BSA, and incubated with  
733 mouse anti-HA-Alexa-594 (1:200) and 4',6-diamidino-2-phenylindole (DAPI), diluted to 1 µg/ml for 2  
734 hr RT. Cells transfected with M-FLAG, E and N were stained overnight with mouse anti-BST-2 (diluted  
735 1:300 in 1% BSA in PBS). The following day the cells were washed 3x PBS and incubated with donkey  
736 anti-mouse-Rhodamine-Red-X (1:400) for 2 hr RT. The cells were washed 3x PBS (10 min per wash)  
737 and blocked with 2% BSA in PBS supplemented with 5% normal mouse serum for 1 hr RT, briefly washed  
738 in 2% BSA, and incubated with rat anti-FLAG-Alexa-488 (diluted 1:200) and 1 µg/ml DAPI  
739 for 2 hr RT. Cells transfected with Orf7a-3xFLAG were stained overnight with mouse anti- HM1.24  
740 (diluted 1:300). The following day the cells were washed 3x PBS and incubated with donkey anti-  
741 mouse-Rhodamine-Red-X (1:400) for 2 hr RT. The cells were washed 3x PBS (10 min per wash) and  
742 blocked with 2% BSA in PBS supplemented with 5% normal mouse serum for 1 hr RT, briefly washed  
743 in 2% BSA, and incubated with rat anti-FLAG-Alexa-488 (diluted 1:200) and 1 µg/ml DAPI for 2 hr  
744 RT. Following immunostaining, the cells were washed extensively in PBS, and briefly in distilled-water,  
745 before mounting in Mowiol (Polyvinyl alcohol) mounting medium (prepared in-house). *Microscopy:*  
746 Images were captured at 100x magnification (1344 ×1024 pixels) using an Olympus IX81 widefield  
747 microscope fitted with a Hamamatsu CCD camera. For each field, a Z-series of images was collected,  
748 deconvolved using the nearest-neighbor algorithm (Slidebook software V.6, Imaging Innovations, Inc)  
749 and presented as Z-stack projections. Inset images are deconvolved single z-section images. Arrow  
750 heads indicate areas of colocalization, scale bar = 10 µm. Image brightness was adjusted using Adobe  
751 Photoshop CS3.  
752

753 **FIGURE LEGENDS**

754

755 **Figure 1 - IFN-mediated restriction of SARS-CoV-2 relies on a limited subset of ISGs**

756 (A) Schematic representation of the gain-of-function screen to identify ISGs that inhibit SARS-CoV-2  
757 replication. (B) Ranked log2FC SARS-CoV-2 infectivity values (blue shading) and normalized cell  
758 number (pink shading), after individual overexpression of 399 human ISGs and controls. Dashed lines  
759 illustrate cut offs for antiviral ISG hit calling strategy: dotted blue line, infectivity = 4\*Stdev log2FC  
760 *CAT*; dotted pink line, cell viability = 70% of *CAT*. Controls are shown (*CAT*, negative; *LY6E*, positive).  
761 (C) Correlation plots of log2FC infectivity values for ISG overexpression screens using 293T cells  
762 infected with SARS-CoV-2. r = Pearson correlation coefficient between screens. (D) 293T-ACE2 stably  
763 expressing each of the identified ISGs were infected with SARS-CoV-2 (MOI 0.25). At 40 h post-  
764 infection, cells were fixed, stained with DAPI and immunolabelled with anti-SARS-CoV-2  
765 nucleoprotein (N) antibody. Log2FC infectivity was calculated as the percentage of N<sup>+</sup>/DAPI<sup>+</sup> cells  
766 relative to parental control wells. Data represent mean ± SD of three independent experiments (n=3).  
767 Statistical significance was calculated using one-way ANOVA with Sidak's multiple comparison post-  
768 hoc test. Representative images are shown in (E). Scale bar = 10 μm.  
769

#### 770 **Figure 2 – Network model of SARS-CoV-2 antiviral effectors**

771 (A) The network containing the 65 identified antiviral ISGs was expanded to include a total of 343 high  
772 confidence protein interactors (Score> 0.7 STRING) and subjected to supervised community detection  
773 (Carlin et al., 2017; Shannon, 2003). The resultant hierarchy is shown. Here, each node represents a  
774 community of densely interconnected proteins, and each edge (arrow) denotes containment of one  
775 community (edge target) by another (edge source). Enriched biological processes are indicated. The  
776 percentage of each community that corresponds to the 65 antiviral ISGs is shown in dark blue. (B-E)  
777 Zoom-in insets from selected protein communities are indicated with an asterisk \* in the hierarchy.  
778 Nodes indicate proteins, and edges indicate interactions from STRING. Blue nodes indicate ISGs that  
779 restricted SARS-CoV-2 replication.  
780

#### 781 **Figure 3 – SARS-CoV-2 antiviral effectors inhibit discrete viral replication steps**

782 293T-ACE2 cells stably expressing each of the indicated ISGs were subjected to (A) infection with  
783 SARS-CoV-2 pseudotyped VSV luciferase virus (VSV-S-luc) for 16 h prior to measurement of  
784 luciferase signal. In parallel, cells were subjected to synchronized infection with SARS-CoV-2 (MOI =  
785 4) for 6 h prior to measurement of viral RNA (B), or supernatants at 18 h post-infection were used to  
786 infect naïve Vero E6 cells. Infectivity was then determined at 18 h post-infection using immunostaining  
787 for viral N protein (C). In parallel to these experiments, the impact of these ISGs in 293T-ACE2 cells  
788 on SARS-CoV-2 replication at 24 h post-infection was evaluated (full lifecycle). Results are summarized  
789 in the heat map and show the mean (n=2) of relative activities compared to parental cells.  
790

#### 791 **Figure 4 – Integrated model of SARS-CoV-2 cellular restriction mechanisms**

792 ISGs that inhibited SARS-CoV-2 replication were placed at specific positions along the viral infectious  
793 cycle based on experimental data generated in Figure 3 in conjunction with Gene Ontology, KEGG,  
794 Reactome databases and the literature. Human ISGs are represented in blue, and SARS-CoV-2 proteins  
795 in yellow. Asterisks \* indicate ISGs that were validated using lentiviral transduction. Dashed lines  
796 (edges) represent indirect interactions between these ISGs and the indicated viral proteins based on  
797 constitutively expressed interactors of ISGs (Hubel et al., 2019) and reported SARS-CoV-2 interactors  
798 (Gordon et al., 2020).

799

800 **Figure 5 – BST2 inhibits release of SARS-CoV-2 and is antagonized by Orf7a**

801 (A, B) 293T and Huh7 cells transfected with BST2 along with ACE2 and TMPRSS2 were infected with  
802 SARS-CoV-2 at the indicated MOIs for 48 h prior to immunostaining for viral N protein. Shown is  
803 quantification of infectivity (% infected cells) relative to empty vector control (A), and representative  
804 images of Huh7 cells infected at MOI 0.03 (B). Data show mean ± SD from three independent  
805 experiments. (C) HeLa-ACE2 parental or BST2 KO cells were infected with SARS-CoV-2 (MOI = 2).  
806 At the indicated hours post-infection, supernatants were collected and analyzed by plaque assay in Vero  
807 E6 cells. LoD = limit of detection. Data show mean ± SD from one representative experiment in triplicate  
808 (n=3) of two independent experiments. (D) 293T cells were transfected with M-FLAG, E-V5, N-V5,  
809 along with the indicated constructs expressing BST2, human codon-optimized HIV-1 Vpu and/or  
810 FLAG-tagged SARS-CoV-2 Orf7a. At 24 h post-transfection, cell lysates and supernatants (VLPs) were  
811 analyzed using SDS-PAGE and immunoblotted with indicated antibodies. (E) HeLa-ACE2 cells  
812 transfected with M-FLAG, E, and N, were subjected to immunostaining for BST2 and FLAG, as  
813 indicated. Shown are deconvolved widefield microscopic images revealing colocalization of BST2 and  
814 M (arrows). Scale bar = 10 µm. (F) HeLa-ACE2 cells transfected with Orf7a-FLAG were subjected to  
815 immunostaining for BST2 and FLAG, as indicated. Shown are confocal images revealing colocalization  
816 of BST2 and Orf7a (arrows). Scale bar = 10 µm. (G) Parental 293T-ACE2 or BST2 stable cells were  
817 infected with WT or dOrf7a (MOI = 1). At indicated times post-infection, supernatants were collected  
818 and analyzed by plaque assay in VeroE6 cells. Data show mean ± SD from one representative  
819 experiment in triplicate (n=3) of two independent experiments. Statistical significance was calculated  
820 using one-way ANOVA with Dunnet's post-hoc (A), Student's t-test (C), or Tukey's multicomparison  
821 test (G).

822

823 **Figure 6 – Comparative antiviral activities of SARS-CoV-2 restriction factors**

824 Heat map showing normalized infection upon overexpression of indicated ISGs across 21 viruses. Data  
825 for SARS-CoV-2 were generated within this study. Data for the remaining 20 viruses were obtained  
826 from previously published work (Schoggins et al., 2011, 2014). Virus families are indicated.  
827 Chikungunya virus (CHIKV), O'nyong'nyong virus (ONNV), Sindbis virus (SINV), Venezuelan equine  
828 encephalitis virus (VEEV), Yellow fever virus (YFV), Human parainfluenza virus type 3 (PIV3),

829 Human metapneumovirus (HMPV), Newcastle disease virus (NDV), Respiratory syncytial virus (RSV),  
830 Measles virus (MV), Equine viral arteritis (EVA), Bunyamwera virus (BUNV), poliovirus (PV),  
831 coxsackievirus (CBV), vaccinia virus (VV).  
832

Figure 1

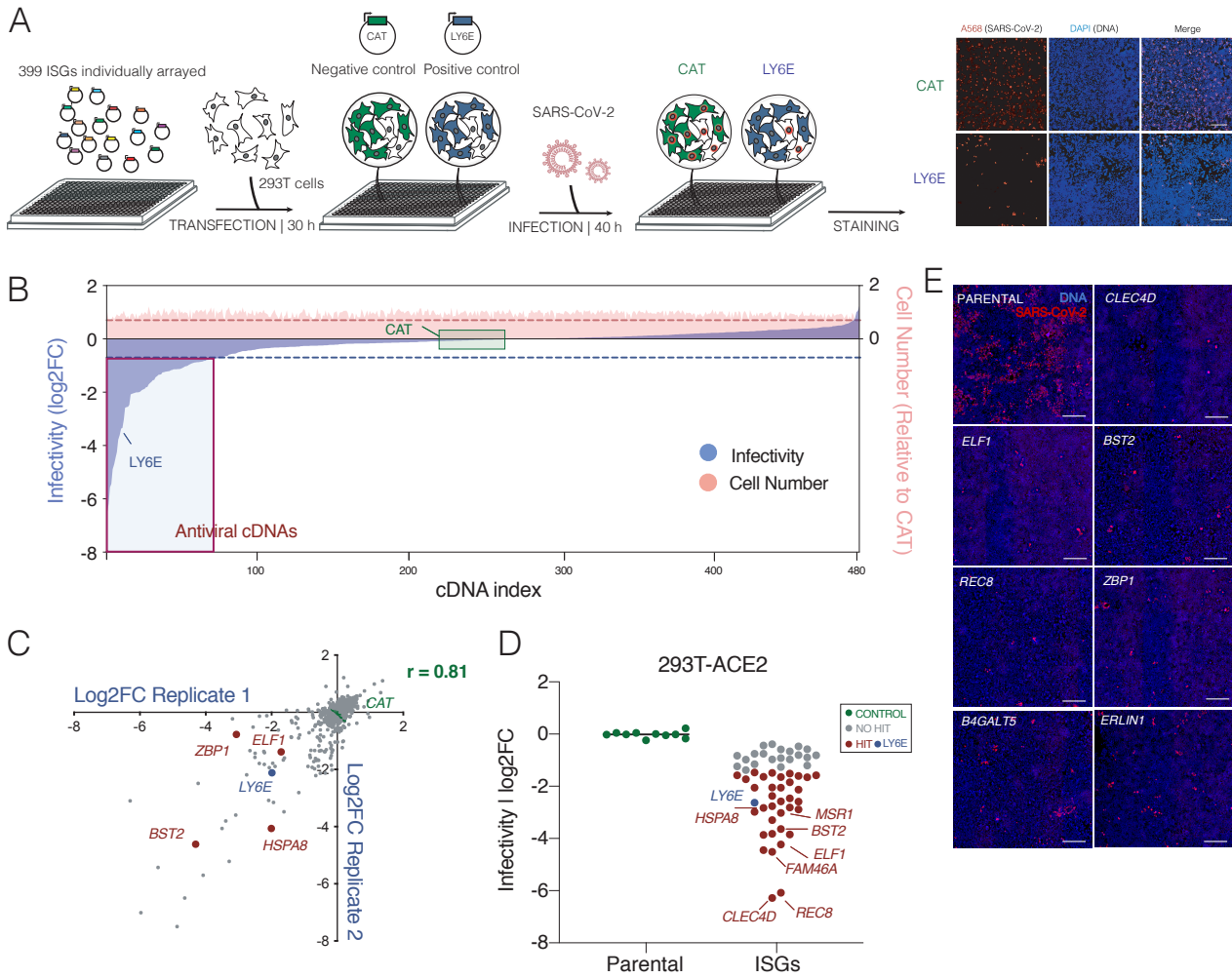


Figure 2

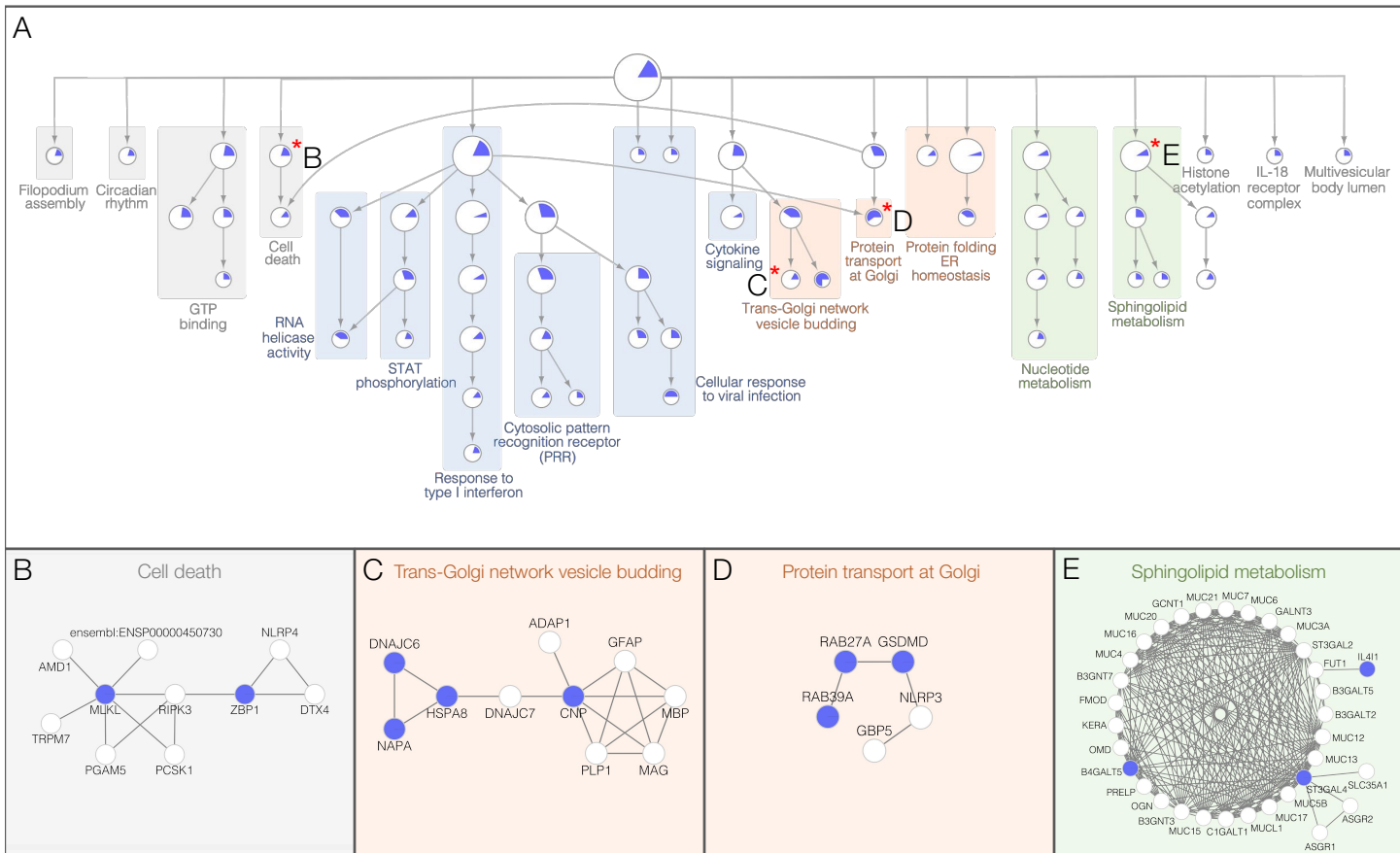


Figure 3

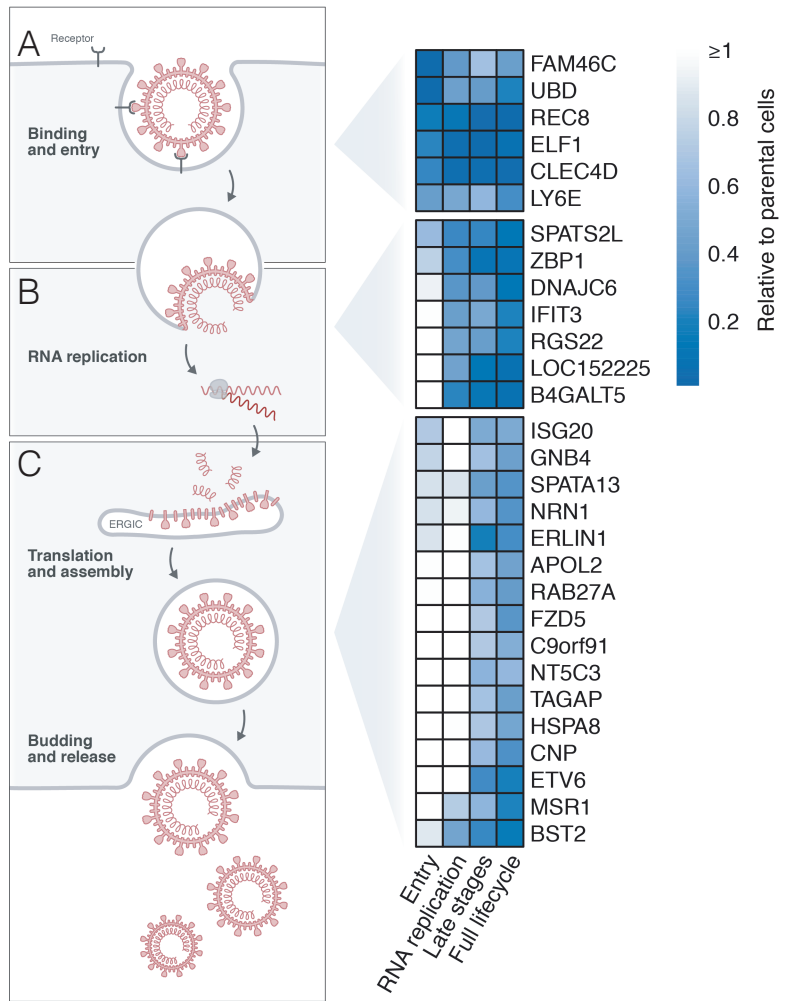


Figure 4

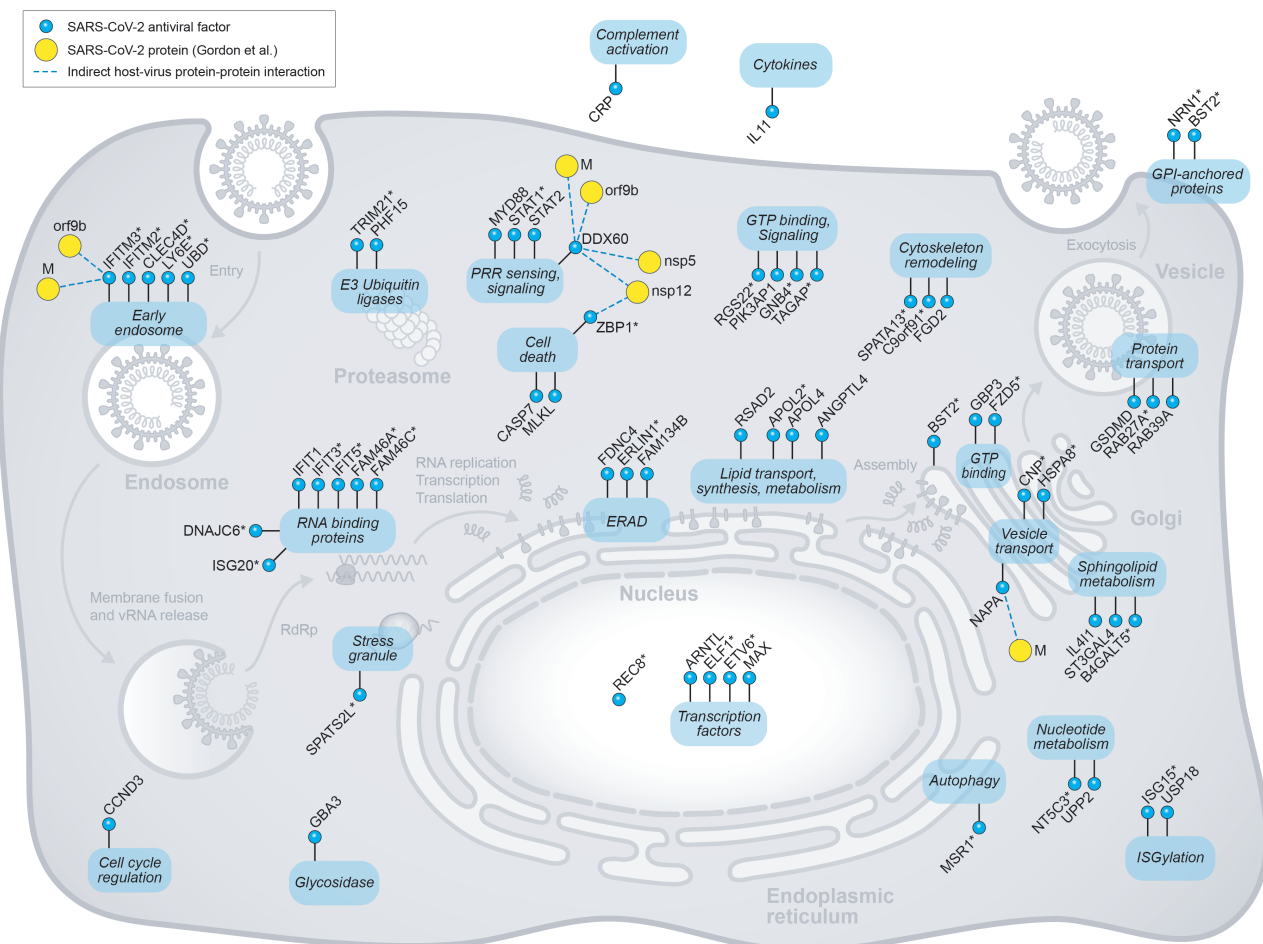
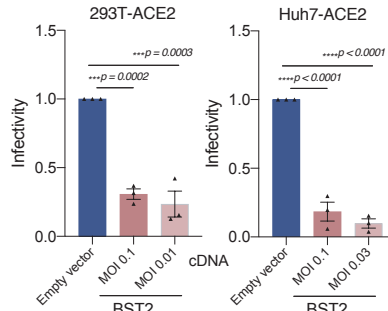
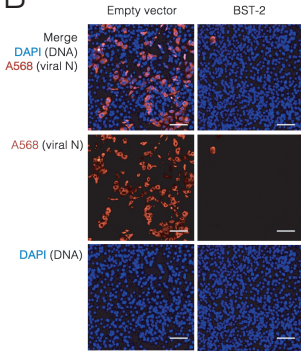


Figure 5

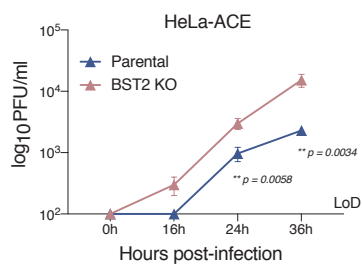
A



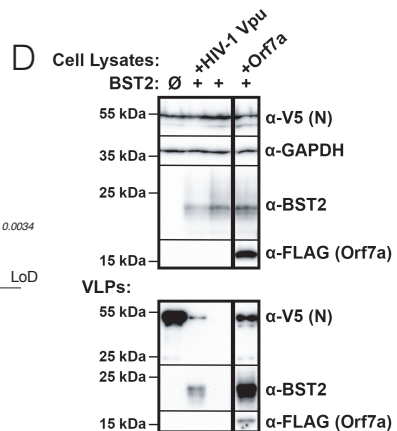
B



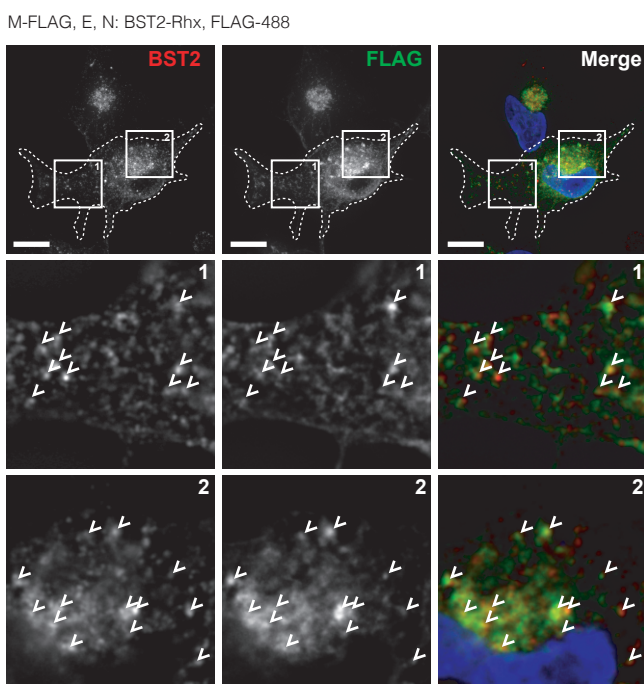
C



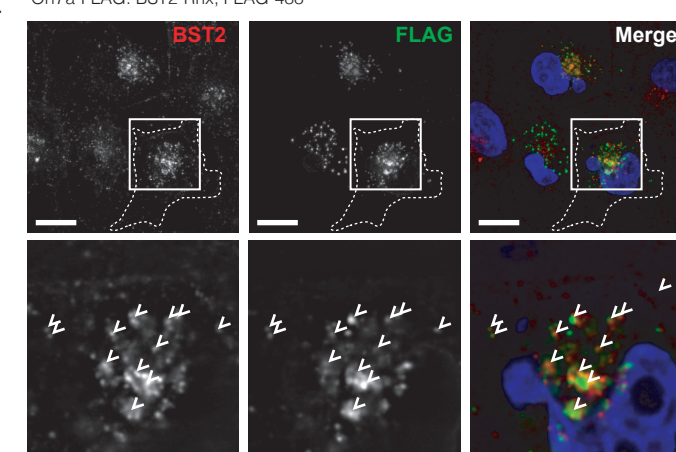
D



E



F



G

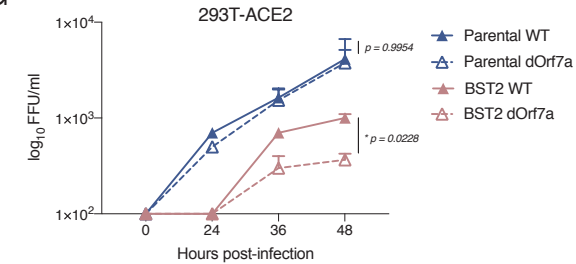


Figure 6

